Classical density functional theory for a two-dimensional isotropic ferrogel model with labeled particles

Segun Goh,[*] René Wittmann, Andreas M. Menzel, and Hartmut Löwen[†]

Institut für Theoretische Physik II: Weiche Materie, Heinrich-Heine-Universität Düsseldorf, 40225 Düsseldorf, Germany

In this study, we formulate a density functional theory (DFT) for systems of labeled particles, considering a two-dimensional bead-spring lattice with a magnetic dipole on every bead as a model for ferrogels. On the one hand, DFT has been widely studied to investigate fluidlike states of materials, in which constituent particles are not labeled as they can exchange their positions without energy cost. On the other hand, in ferrogels consisting of magnetic particles embedded in elastic polymer matrices, the particles are labeled by their positions as their neighbors do not change over time. We resolve such an issue of particle labeling, introducing a mapping of the elastic interaction mediated by springs onto a pairwise additive interaction (pseudosprings) between unlabeled particles. We further investigate magnetostriction and changes in the elastic constants under altered magnetic interactions employing the pseudospring potential. It is revealed that there are two different response scenarios in the mechanical properties of the dipole-spring systems: While systems at low packing fractions are hardened as the magnetic moments increase in magnitude, at high packing fractions softening due to diminishing effects from the steric force, associated with increases in the volume, is observed. The validity of the theory is also verified by Monte Carlo simulations with both real springs and pseudosprings. We expect that our DFT approach may promote our understanding of materials with particle inclusions.

I. INTRODUCTION

In statistical mechanics, *indistinguishability* of particles and consequently the correct Boltzmann counting play an essential role (see, e.g., Refs. [1–3]). The Gibbs paradox is well known in this regard and the extensivity of entropy is recovered by introduction of the $1/N!$ factor, which corrects the number of microstates by the number of permutations of N particles. Commonly, the $1/N!$ factor is regarded as a remnant of quantum mechanics in the classical limit, in which identical particles are inherently indistinguishable. In contrast to such a point of view, however, the $1/N!$ factor should be consistently interpreted based on an informatic definition of entropy [4]. Accordingly, a modified term, "undistinguished" particles [5], has also been proposed. Consequently, even though the classical particles such as colloidal particles are undoubtedly distinguishable, the statistical mechanics with the $1/N!$ correction describes the macroscopic behaviors of such systems successfully [6,7], as long as one ignores detailed differences between particles [8,9] and leaves the particles unlabeled.

At the very microscopic level, i.e., at the atomic scale, a system consisting of identical particles is invariant under permutations of the particles and the particles are unlabeled in principle. If one considers a mesoscopic length scale and employs a coarse-grained description [10,11], however, it may become necessary to distinguish between particles that are physically identical. Such a scenario can emerge if

the particles are permanently localized with respect to their neighbors, thereby rendering the system nonergodic on the relevant energy scale. It is thus a major challenge for statistical mechanical theories to describe a model with labeled particles [12] or to keep track of a single localized particle [13].

Here we develop a statistical description for a class of composite materials, which consist of magnetic particles and an elastic polymer matrix [11,14,15]. In these materials, called ferrogels or magnetorheological elastomers, the dynamical trajectories of the magnetic particles are frequently strongly constrained by the polymeric environment [16,17]. Such a magnetomechanical coupling can even be enhanced by directly anchoring the polymers on the surface of magnetic particles [15,18–20]. Hence, the elastic properties of the materials can be tuned from the outside by noninvasive applications of magnetic fields [21–23]. As a further consequence of this coupling, the particles cannot exchange their positions due to the fixation by the elastic medium.

Various studies have been conducted to understand theoretically the behavior of such ferrogels with different description levels from the microscopic scale resolving the individual polymer particles to the macroscopic hydrodynamic or thermodynamic theory. For many practical purposes, one may neglect the thermal motions of the magnetic particles [11]. In particular, a mesoscopic dipole-spring model has been adopted to study the elastic and dynamical properties of ferrogels [24–26]. The matrix-mediated interaction between magnetic particle inclusions has also been revealed in terms of continuous elastic backgrounds [27–32]. Furthermore, microscopic descriptions of ferrogels via coarse-grained molecular dynamics simulations enable us to probe the role of thermal motions of the magnetic particles explicitly [33–35].

─────────
[*]segun.goh@hhu.de
[†]hlowen@thphy.uni-duesseldorf.de

Here we merge several of the aspects mentioned above. Our goal is to formulate a statistical mechanical theory for ferrogels in a dipole-spring model with thermal fluctuations of the magnetic particles taken into account. The most challenging problem that has to be addressed along the way arises from the fact that the particles in ferrogels are strictly *labeled* by their positions as in lattice systems, for instance, the classical Ising or *XY* models [36] and harmonic crystals [37]. Accordingly, correcting the number of microstates by the factor $1/N!$ does not apply to a statistical description of ferrogels and a permutation of particles will cause a change in energy (physically this results in strong distortions of the surrounding elastic matrix). While computational approaches such as Monte Carlo (MC) simulations are still feasible [35], the formulation of a statistical mechanical theory is severely complicated by the inherent composite nature of the ferrogels, in contrast to, for instance, harmonic crystals. In practice, one would need to take into account the nonlinearity stemming from the steric and magnetic interactions.

One natural candidate for a statistical theory is classical density functional theory (DFT) [38–40], which has been probed to be successful for a variety of systems [41], ranging from simple classical fluids [42] to systems showing a freezing transition [43], from hard spheres [44] to hard convex particles [45], and also for two-dimensional systems [46–48], including dipolar or electrostatic interactions [49,50], and capturing the spinodal decomposition dynamics [51] in an adiabatic approximation for time-dependent systems. However, due to the particle labeling, a direct application of the machinery of DFT to ferrogels is not possible. To this end, we will map the elastic interaction onto an appropriate pairwise pseudopotential [12] between unlabeled particles, which allows us to formulate a DFT. Ultimately, we aim at investigating the elastic properties of the dipole-spring systems within the DFT framework. By comparison to the MC simulations, the validity of the theory is confirmed.

The paper is organized as follows. In Sec. II we introduce a two-dimensional model for ferrogels. Section III describes detailed procedures of the mapping and the subsequent formulation of a DFT. Combining MC simulations and DFT calculations, two distinctive response scenarios in elastic properties to the change of the magnetic moment are identified in Sec. IV. A summary and a discussion are given in Sec. V.

II. DIPOLE-SPRING MODEL

We consider a bead-spring model [10] in terms of a periodic two-dimensional hexagonal lattice, as illustrated in Fig. 1. There are N identical magnetic particles and $3N$ identical harmonic springs connecting the nearest neighbors. We denote the position and the dipole moment of the ith particle of diameter σ by $\vec{r}_i$ and $\vec{m}_i$, respectively. The total Hamiltonian $\mathcal{H}_{\text{tot}}$ of the model system is given by the sum of the kinetic part and the interaction Hamiltonian $\mathcal{H}_{\text{int}}$, which consists of three parts in the form

$$\mathcal{H}_{\text{int}} = \mathcal{H}_{\text{m}} + \mathcal{H}_{\text{el}} + \mathcal{H}_{\text{st}}. \tag{1}$$
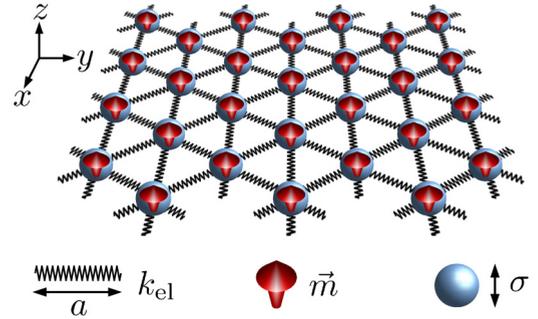
FIG. 1. Illustration of the dipole-spring model.

Among these three terms, the magnetic part $\mathcal{H}_{\text{m}}$ and the steric part $\mathcal{H}_{\text{st}}$ can be written as

$$\mathcal{H}_{\text{m,st}} = \frac{1}{2} \sum_{i \neq j} u_{\text{m,st}}(\vec{r}_{ij}), \tag{2}$$

where $\vec{r}_{ij} = \vec{r}_j - \vec{r}_i$. For isotropic interactions, the vector $\vec{r}_{ij}$ in the argument can be replaced by $r_{ij} = |\vec{r}_{ij}|$.

First, the two-body magnetic dipole-dipole interaction energy between magnetic particles reads

$$u_{\text{m}}(\vec{r}_{ij}) = \frac{\mu_0}{4\pi} \left[\frac{\vec{m}_i \cdot \vec{m}_j}{r_{ij}^3} - \frac{3(\vec{m}_i \cdot \vec{r}_{ij})(\vec{m}_j \cdot \vec{r}_{ij})}{r_{ij}^5} \right], \tag{3}$$

where μ_0 is the vacuum permeability. Henceforth, we assume that the magnetic moment is constant in time and for all particles, i.e., $\vec{m}_i(t) = \vec{m}$ regardless of i and t, for the sake of simplicity. Moreover, we constrain ourselves to isotropic magnetic interactions in the two-dimensional plane by further assuming that $\vec{m} = m\hat{z}$ is perpendicular to the lattice plane so that the magnetic two-body interaction energy can be written in a simpler form as

$$u_{\text{m}}(r_{ij}) = \frac{\mu_0 m^2}{4\pi} \frac{1}{r_{ij}^3}. \tag{4}$$

The second term in Eq. (1) corresponds to the elastic energy of the harmonic springs and reads

$$\mathcal{H}_{\text{el}} = \sum_{\langle i,j \rangle} u_{\text{el}}(r_{ij}) = \sum_{\langle i,j \rangle} \frac{1}{2} k_{\text{el}} (r_{ij} - a)^2, \tag{5}$$

where k_{el} is the spring constant and a is the rest length of the springs. Apparently, each spring connects a certain prescribed pair of particles, and our summation consistently runs only over nearest-neighboring pairs as indicated by the angular bracket. Consequently, all particles are labeled by the predetermined ordering on a lattice, the energetic memory of which is recalled by $\mathcal{H}_{\text{el}}$. We remark that Eq. (5) cannot be cast into the form of $\frac{1}{2} \sum_{i \neq j} \bar{u}_{\text{el}}(\vec{r}_{ij})$ with an (i, j)-independent function $\bar{u}_{\text{el}}(\vec{r})$.

Finally, the two-body steric repulsion energy is taken as a hard-core potential of the form

$$u_{\text{st}}(r_{ij}) = \begin{cases} 0 & \text{if } r_{ij} \geqslant \sigma \\ \infty & \text{otherwise} \end{cases} \tag{6}$$

and completes the interaction Hamiltonian in Eq. (1). This term prevents the possible divergence of the magnetic

interactions at $r_{ij} = 0$. Following Refs. [46,48,52,53], we introduce a dimensionless packing fraction defined as the ratio of the space occupied by particles to the two-dimensional "volume" of the system (the term volume is used for area throughout the paper). As we might consider the systems under constant pressure (see Sec. IV A), however, the volume V of our system is not necessarily a fixed variable. We therefore define a reference volume $V_{ref} \equiv N V_0 \equiv N \sqrt{3} a^2 / 2$ in which the springs are in their rest state. Accordingly, the packing fraction of a reference system with this volume is given by $\eta_0 = (\sigma^2 \pi / 2) / \sqrt{3} a^2$. Apart from a, which will be used as the unit of length, η_0 depends only on the diameter of particles σ and therefore we employ it as a model parameter representing the steric repulsion. In contrast to that, the conventional packing fraction $\eta \equiv (\pi \sigma^2 / 4) N / V$ defined in terms of the "actual" volume V of the system may change as the volume increases (decreases) in response to a decrease (increase) of the pressure or an increase (decrease) of the magnetic moment m at constant pressure.

From now on, we measure lengths and energies in units of a and $k_B T$, respectively. Accordingly, the magnetic moment m and the spring constant k_{el} are measured in units of $m_0 \equiv \sqrt{k_B T a^3 / \mu_0}$ and $k_B T / a^2$, respectively. Finally, let us note that our bead-spring model is identical to the classical harmonic crystal [37] if the magnetic interaction energy $\mathcal{H}_m$ and the steric repulsion energy $\mathcal{H}_{st}$ are neglected in Eq. (1).

III. MAPPING ONTO PSEUDOSPRINGS

Now we address the issue of particle labeling and derive an approximate elastic Hamiltonian $\tilde{\mathcal{H}}_{el}$, which can be readily used for the density functional calculation. Putting aside the magnetic and steric parts of the Hamiltonian, i.e., $\mathcal{H}_{m,st}$, which are free from this issue [see Eq. (2)], we consider only the elastic part $\mathcal{H}_{el}$ in this section. Following Ref. [12], we consider a mapping of $\mathcal{H}_{el}$ onto a pseudospring potential between unlabeled particles of the form

$$\mathcal{H}_{el} \rightarrow \tilde{\mathcal{H}}_{el} = \frac{1}{2} \sum_{i \neq j} u_{pel}(r_{ij}), \qquad (7)$$

where $u_{pel}(r)$ is a two-body interaction between particles of center-to-center distance r. In contrast to Eq. (5), here $\tilde{\mathcal{H}}_{el}$ involves all particle pairs (i, j). Consequently, the Hamiltonian $\tilde{\mathcal{H}}_{el}$ is invariant under permutations of the particles, i.e.,

$$\tilde{\mathcal{H}}_{el}(\{\vec{r}_i\}) = \tilde{\mathcal{H}}_{el}(\{\vec{r}_{\hat{\pi}(i)}\}), \qquad (8)$$

where $\hat{\pi}$ is a permutation operator constituting the symmetric group S_N. While such a mapping is convenient from a technical point of view, it is physically appropriate only if we can ensure through the form of $u_{pel}(r)$ that each particle in effect interacts only with a prescribed set of other particles, i.e., the same number of nearest neighbors as in the real-spring system. To this end, we will cut each springlike interaction (which we specify later) at larger distances to prevent interactions between particles too far away from each other. The crucial point is then to ensure that $\tilde{\mathcal{H}}_{el}$ neither introduces additional contacts nor misses actually existing ones.

In one spatial dimension, the particles described by a pseudospring model are automatically "labeled" through the
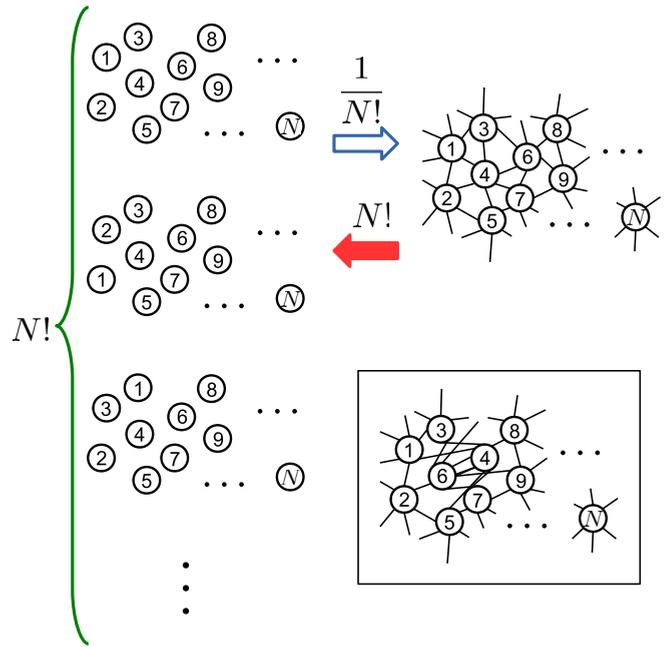
FIG. 2. Mapping between the systems of unlabeled particles with pseudopotential interaction (left-hand side) and labeled particles linked by springs (right-hand side). In the former case, there are $N!$ equivalent microscopic states that correspond to a single overall structure. In sharp contrast to that, in the latter case, permutations of particle positions (keeping the springs intact and thus leading to strong distortions) indeed involve changes in energy, as depicted in the inset.

steric hard-core repulsion [54,55], which fixes their mutual ordering. Hence, within a proper range of the spring length at sufficiently high density [12], where the particles usually interact with their two nearest neighbors, the mapping works perfectly. Note that there is no phase transition due to the strong thermal fluctuations in one dimension. In a more realistic two- or three-dimensional fluid, however, the particles can always find a path to bypass each other. Still, a fixation similar to a cell surrounded by the nearest neighbors can be achieved via ergodicity breaking associated with the freezing transition. In this sense, we can construct a mapping of the labeled particles in the original lattice model onto the crystalline phase of the unlabeled particles with all-to-all pairwise-additive interactions. We take this viewpoint as the inversion of the following interpretation from Ref. [4] for a system of unlabeled hard spheres. For hard-sphere crystalline systems, even though there are $N!$ possible distinct crystals of labeled particles as the Hamiltonian is invariant under permutations, all microscopic configurations correspond to one unique overall lattice structure, as depicted in Fig. 2 (blue open arrow). In this way, lattice models of labeled particles, for which the $1/N!$ factor is omitted in the statistical counting, provide a good approximation for the crystalline state of materials, emerging from the freezing of fluids with unlabeled particles. Inversely, for ferrogels, given the lattice system of labeled particles as the original model, we restore the $1/N!$ factor when we map the unique lattice onto $N!$ possible frozen states of a fluidlike system with unlabeled particles, as represented by the red closed arrow in Fig. 2.
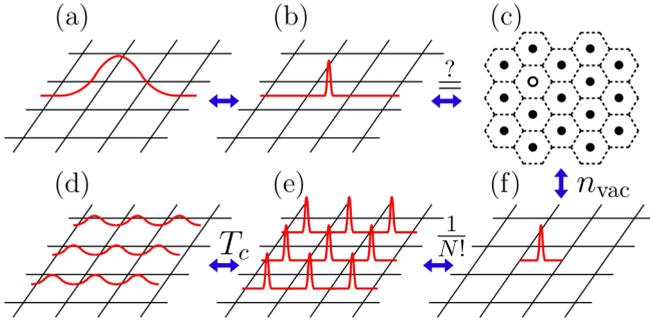
FIG. 3. Schematic diagram to illustrate the justification of our mapping. (a), (b), and (d)–(f) Whole $4N$-dimensional phase space partitioned by the black grids, each cell of the grid representing a permutation-related subspace σ_i. Probability density profiles in the phase space are depicted by red lines. Specifically, the probability densities of the real-spring systems at (a) high and (b) low temperature are illustrated, as well as those using pseudosprings at (d) high and (e) low temperature. (f) One density profile, localized within one single permutation-related subspace, is chosen arbitrarily from $N!$ available subspaces [the $1/N!$ factor is simultaneously omitted in the partition function; see the last equality in Eq. (10)]. Moreover, (c) describes the lattice structure in the configurational space corresponding to (f) [see Eq. (10)] or approximately to (b) [see Eq. (9)]. Finally, the approximation involved in between (b) and (c) is optimized via Eq. (11), which we here achieve by searching for a vanishing concentration n_{vac} of vacancies [indicated by an open circle in (c)].

In Sec. III A and in Fig. 3, our argument justifying such a mapping in two dimensions is laid out in full detail, before establishing the specification of the elastic pseudopotential u_{pel} in Sec. III B. Then we demonstrate in Sec. III C how to implement the mapped system within our DFT approach. Before we proceed, we make two additional remarks. First, we assume that the pseudospring systems governed by u_{pel} have a crystalline phase. Second, we consider two-dimensional crystals [56,57] in this study. As is well known, there is no true long-range order in two-dimensional systems in the absence of truly long-range interactions [58].

A. Detailed justification of the mapping

Our argument is based on the idea that, at low temperatures, the energetic contribution overwhelms the entropic contribution involving the $1/N!$ factor, enabling us to map the systems of labeled particles onto those of the unlabeled ones. Such an argument is strong enough to justify the mapping, for instance, at zero temperature, for which the minimum of $\mathcal{H}_{\text{int}}$ completely determines the equilibrium properties. At finite temperatures, however, the elastic properties (or even the stability of the systems) critically depend on the details of the mapping and of the profile of the consequent interaction potential $\tilde{\mathcal{H}}_{\text{int}} \equiv \mathcal{H}_{\text{m}} + \tilde{\mathcal{H}}_{\text{el}} + \mathcal{H}_{\text{st}}$. This applies not only at the minimum of $\tilde{\mathcal{H}}_{\text{int}}$, but even if the adjacent particles are not located exactly at their lattice sites due to thermal fluctuations. Accordingly, a quantitative matching of lattice structures in real-spring and pseudospring systems turns out to be essential. Therefore, in this section, we carefully describe how the $1/N!$ factor and the fluctuations of particles confined to their

lattice sites in the low-temperature crystalline phase should be addressed throughout the mapping.

Let us consider the $4N$-dimensional phase space of our system. The probability density to locate our system in this phase space reads $\omega(\{\vec{r}_i\}, \{\vec{p}_i\}) \propto \exp[-\beta \mathcal{H}_{\text{tot}}(\{\vec{r}_i\}, \{\vec{p}_i\})]$ with the conventional definition $\beta \equiv k_B T$. We then partition the phase space into $N!$ subspaces that are related by permutations of the particles, analogously to the symmetry-related regions discussed in Ref. [36]. To this end, we first specify the completely ordered set (subspace) as $\sigma_1 = \{(\vec{r}_1, \ldots, \vec{r}_N, \vec{p}_1, \ldots, \vec{p}_N) \mid |\vec{r}_i| > |\vec{r}_j|, \ i > j\}$. In other words, every configuration in which each particle with a smaller label is located closer to the origin than each of the other particles with a larger label belongs to this subspace. (If there exist pairs of particles, whose distances from the origin are the same, one can further order the particle pairs by comparing the angle, e.g., from the x axis.) Then, with the permutation operators $\hat{\pi}_i$ (for $i = 1, \ldots, N!$ where $\hat{\pi}_1$ is the identity of the S_N symmetric group) introduced in Eq. (8), one can generate $N!$ subspaces exhausting the whole phase space by permuting particles, i.e., $\sigma_i = \{(\vec{r}_{\hat{\pi}_i(1)}, \ldots, \vec{r}_{\hat{\pi}_i(N)}, \vec{p}_{\hat{\pi}_i(1)}, \ldots, \vec{p}_{\hat{\pi}_i(N)}) \mid (\vec{r}_1, \ldots, \vec{r}_N, \vec{p}_1, \ldots, \vec{p}_N) \in \sigma_1\}$. For example, a subspace σ_α is generated by the permutation of particles of the completely ordered subspace σ_1, with a corresponding operator $\hat{\pi}_\alpha$.

In the case of the real-spring systems, the probability densities of each subspace are not identical to each other [see Figs. 3(a) and 3(b)], as an exchange of any particle pair is always accompanied by a change in energy, i.e., $\mathcal{H}_{\text{el}}(\{\vec{r}_i\}) \neq \mathcal{H}_{\text{el}}(\{\vec{r}_{\hat{\pi}(i)}\})$. However, for pseudospring systems, the probability densities corresponding to each subspace are identical to each other, as illustrated in Figs. 3(d) and 3(e), because the Hamiltonian is invariant under permutations. Therefore, the probability densities in the whole phase space of the real-spring and pseudospring systems are not equivalent to each other in general. More specifically, for real-spring systems, the probability density in a subspace should deviate from the one in another subspace as they involve permutations of particles, while for pseudospring systems they are still identical due to the symmetry under permutations.

Let us now turn to low-temperature systems, i.e., $k_B T \ll k_{\text{el}} a^2$. Recall that there is no phase transition for harmonic crystals [37,59], that is, for our real-spring system. Nonetheless, the corresponding probability density becomes highly localized, as depicted in Fig. 3(b). In the case of the pseudospring system, a freezing transition might occur instead, which is the starting point of our mapping. First we constrain ourselves to each one of the permutation-related subspaces. Therefore, particle exchanges or, namely, permutations of particles via, e.g., vacancy hopping are ignored in the following analysis. Then we consider the ergodicity breaking of the systems due to freezing. Accordingly, the probability density in each permutation-related subspace is isolated as illustrated in Fig. 3(e). [In contrast to that, as shown in Figs. 3(a) and 3(d), the probability densities at high temperature are rather broad for both the real- and pseudospring systems and therefore it is not possible to construct such a mapping in our situation.] In both systems, we conclude that, below a certain temperature, the thermal vibration in the particle positions is much smaller than interparticle distances in the crystalline state. Therefore, the trajectory of each particle in

each subspace does not span the full configurational space $\mathbb{R}^2$ but only a localized area. That is, a particle i remains localized within the corresponding Wigner-Seitz cell Ω_i associated with its average position [see Fig. 3(c)]. In such a way, we provide a tiling of $\mathbb{R}^2 = \Omega_1 \cup \cdots \cup \Omega_N$, where $\Omega_i \cap \Omega_j = \emptyset$ for $i \neq j$.

Now let us be more explicit and consider only one subspace among all permutation-related subspaces at low temperature. In the case of the real-spring system, a particle i is localized in the Wigner-Seitz cell around a lattice site with the same label i, so $\int_{\mathbb{R}^2} d\vec{r}_i e^{-\beta \mathcal{H}} \approx \int_{\Omega_i} d\vec{r}_i e^{-\beta \mathcal{H}}$. Then the partition function becomes

$$
\begin{aligned}
Z_N^{\text{real}} &= \frac{1}{\Lambda^N} \int_{\mathbb{R}^2} d\vec{r}_1 \cdots \int_{\mathbb{R}^2} d\vec{r}_N e^{-\beta \mathcal{H}_{\text{int}}} \\
&\to \frac{1}{\Lambda^N} \int_{\Omega_1} d\vec{r}_1 \cdots \int_{\Omega_N} d\vec{r}_N e^{-\beta \mathcal{H}_{\text{int}}},
\end{aligned}
\tag{9}
$$

where Λ is the mean thermal wavelength of the particles. As indicated by the arrow on the second line, the partition function has been rewritten in terms of the Wigner-Seitz cells. With the Wigner-Seitz cells $\{\tilde{\Omega}_i\}$ corresponding to the pseudospring system in the crystalline state, the partition function involving the unlabeled particles can be similarly rewritten as

$$
\begin{aligned}
Z_N^{\text{pseudo}} &= \frac{1}{\Lambda^N N!} \int_{\mathbb{R}^2} d\vec{r}_1 \cdots \int_{\mathbb{R}^2} d\vec{r}_N e^{-\beta \tilde{\mathcal{H}}_{\text{int}}} \\
&\to \frac{1}{\Lambda^N N!} \sum_{\pi \in S_N} \int_{\tilde{\Omega}_{\hat{\pi}(1)}} d\vec{r}_1 \cdots \int_{\tilde{\Omega}_{\hat{\pi}(N)}} d\vec{r}_N e^{-\beta \tilde{\mathcal{H}}_{\text{int}}} \\
&= \frac{1}{\Lambda^N} \int_{\tilde{\Omega}_1} d\vec{r}_1 \cdots \int_{\tilde{\Omega}_N} d\vec{r}_N e^{-\beta \tilde{\mathcal{H}}_{\text{int}}},
\end{aligned}
\tag{10}
$$

where the last equality follows from the fact that $\tilde{\mathcal{H}}_{\text{int}}$ is invariant under permutations. In this way, one can cancel the $N!$ counting factor, completely neglecting the exchange of particles, as illustrated in Fig. 3(f). We stress that the probability of the ignored configurations in both Eqs. (9) and (10) is negligible and vanishes as $T \to 0$ and/or $N \to \infty$.

Comparing now both expressions to each other, we map the lattice of labeled particles to that of unlabeled particles via

$$
\int_{\Omega_1} d\vec{r}_1 \cdots \int_{\Omega_N} d\vec{r}_N e^{-\beta \mathcal{H}_{\text{int}}} = \mathcal{N} \int_{\tilde{\Omega}_1} d\vec{r}_1 \cdots \int_{\tilde{\Omega}_N} d\vec{r}_N e^{-\beta \tilde{\mathcal{H}}_{\text{int}}},
\tag{11}
$$

where $\mathcal{N}$ is an arbitrary constant which does not alter any physical properties of the mapping, indicating that the (many-body) pseudospring potential can be determined up to an additive constant. Even though the above equation is not easy to analyze as it still involves interactions between many particles, the issue of particle labeling has been resolved: The $1/N!$ factor does not appear in the mapping. Moreover, it provides us with a route of how to construct an approximate elastic part of the Hamiltonian $\tilde{\mathcal{H}}_{\text{el}}$ in Eq. (7) for practical calculations. In addition to the trivial condition that (i) the nearest-neighbor interaction of $\mathcal{H}_{\text{int}}$ should be reproduced by $\tilde{\mathcal{H}}_{\text{int}}$, Eq. (11) indicates that (ii) the lattice of the real-spring system should be recovered with the pseudospring potential, namely, $\{\Omega_i\} \stackrel{!}{=} \{\tilde{\Omega}_i\}$. Next we describe our strategy to explicitly perform such a mapping by introducing a cutoff for the springs.

B. Pair potential of pseudosprings

We consider an elastic interaction energy via pseudosprings with a cutoff. The latter introduces an additional degree of freedom to control the offset of the remaining part of the springs, leading to a two-body interaction in the form

$$
u_{\text{pel}}(r_{ij}) =
\begin{cases}
\frac{1}{2} k_{\text{el}} (r_{ij} - a)^2 - u_{\text{pel}}^0 & \text{for } r_{ij} < R_c \\
0 & \text{otherwise,}
\end{cases}
\tag{12}
$$

where k_{el} and a take the same role as in Eq. (5) and the two mapping parameters R_c and u_{pel}^0 are fixed by the conditions (i) and (ii), respectively, as discussed below.

Regarding condition (i), the nature of the mapping onto the pair potential $u_{\text{pel}}(r_{ij})$ leads to an apparent violation of Eq. (11), because the number of nearest neighbors cannot be unambiguously imposed. Even when the potential has only a finite range, additional contacts with next-nearest-neighbor particles can be formed in one direction, simultaneously missing the contacts with nearest-neighbor particles in the other directions. Specifically, if a particle is located, e.g., at one of the corners of its Wigner-Seitz cell, the minimal possible distance to a particle in a nonadjacent cell is only one edge length, i.e., a, while the maximal possible distance to another particle in a neighboring cell is as large as $\sqrt{13}a \approx 3.6a$. This drawback cannot be overcome by any choice of another cell shape but becomes less severe as $k_B T / k_{\text{el}} a^2 \to 0$. Hence, we simply consider an isotropic pseudopotential of range R_c for computational convenience. This cutoff parameter in Eq. (12) should be determined to achieve the optimal connectivity with the six nearest-neighbor particles (see the inset of Fig. 4), as the best approximation for the original bead-spring Hamiltonian.

To this end, we first determine the cutoff radius R_c^0 for the reference system with $V_{\text{ref}} = N V_0$ introduced in Sec. II, in which the springs assume their rest length. As a simple analytic estimate for R_c^0, one may assume a uniform (fluidlike) density N/V_{ref} and replace the seven Wigner-Seitz cells containing a particle and its six nearest neighbors by a circle of the same total area. Such an assumption leads to the value of $R_c^0 = (7V_0/\pi)^{1/2} \approx 1.39a$. As we only consider the crystal, in which the density is highly inhomogeneous, however, R_c^0 is expected to be smaller. As a more appropriate alternative, we extract the value from MC simulations of the real-spring system with $V = N V_0$, i.e., the target of our mapping. Specifically, we compute the isotropic pair correlation function defined as

$$
g(r) = \frac{V}{2\pi r N^2} \left\langle \frac{1}{2} \sum_{i \neq j} \delta(r - r_{ij}) \right\rangle.
\tag{13}
$$

By simply probing the distance at which $g(r)$ takes its first minimum, we find $R_c^0 \approx 1.34a$ (compare Fig. 4). As the effect from the discontinuity of $u_{\text{pel}}(r)$ at R_c^0 (see the solid red line in Fig. 4) is minimized with $R_c^0 = 1.34a$, the convergence rate in DFT calculations turns out to be faster than the minimization with $R_c^0 = 1.39a$ (see Sec. III C). As the results are hardly affected by this small change of the parameter and the value $R_c^0 = 1.34a$ seems to be sufficiently accurate, we use it from now on. For systems under constant pressure with volumes
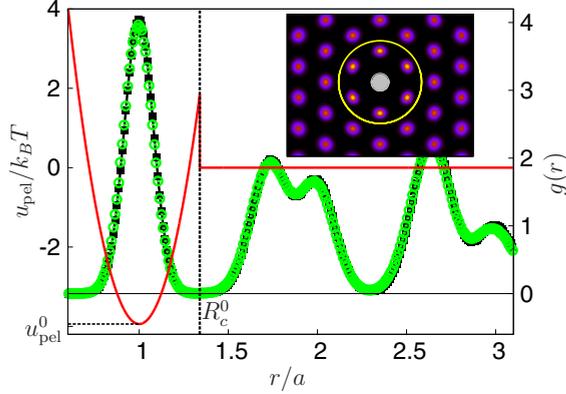
FIG. 4. Agreement between the real-spring and pseudospring systems. We compare pair correlation functions $g(r)$ from the real-spring and pseudospring MC simulations of the reference system with $V = V_{\text{ref}}$, which are depicted by black and green symbols, respectively. First, black squares show $g(r)$ obtained from the MC simulation of the real-spring system. As depicted by the dashed black vertical line, the distance at the minimum point between the first and the second peak in $g(r)$ is chosen as R_c^0. Here $ka^2/k_BT = 100$, $\eta_0 = 0.3$, $m/m_0 = 0$, and $N = 480$ are used and we find $R_c^0 = 1.34a$. In the inset, the anisotropic pair correlation function $g(\vec{r})$ obtained from the real-spring MC-simulation results is also displayed, together with the yellow line indicating R_c^0. As shown, the yellow line is far enough from the neighboring peaks and we confirm that the isotropic cutting off of the springs is a reasonable approach. The pair correlation function $g(r)$ obtained from pseudospring systems with $u_{\text{pel}}^0 = 3.94k_BT$ is represented by green circles. The agreement between the real-spring and pseudospring simulations is manifested clearly. Finally, the solid red line presents the elastic energy of pseudosprings $u_{\text{pel}}(r)$ defined in Eq. (12).

other than $V = V_{\text{ref}}$ (see Sec. IV), we use

$$R_c = R_c^0 \sqrt{\frac{V}{V_{\text{ref}}}}. \tag{14}$$

This is the only external input necessary during the formulation of our DFT in Sec. III C.

Condition (ii) cannot be directly imposed, because the lattice structure is usually not an input but the result of a calculation based on a prescribed interaction. The fact that this condition is not automatically fulfilled even if the real-spring and pseudospring systems are at the same density is related to another aspect of a pair-potential system in general: The lattice may be imperfect, as indicated in Fig. 3(c). The real-spring system with labeled particles assigned to the lattice is completely free from defects, whereas the mismatch between the range of the pairwise interaction and the desired lattice structure suggests that there should be some vacancies or interstitials. Moreover, if there were such defects, Eq. (10) should also be corrected by additional factors addressing the number of possible defect configurations. Hence, we modify $u_{\text{pel}}(r_{ij})$ such that it yields a zero vacancy concentration $n_{\text{vac}} = 0$ as an equivalent requirement to the above condition of an equal cell structure. The only way to do so while leaving R_c invariant is to tune the depth of the pseudospring potential in Eq. (12) by an offset value u_{pel}^0, which we understand as

follows. On the one hand, if $\langle u_{\text{pel}} \rangle \ll 0$, the total elastic energy is lowered by forming additional contacts with new neighbors. This undesired effect results in the undesired formation of interstitials or aggregates. On the other hand, when $\langle u_{\text{pel}} \rangle \gg 0$, vacancies are generated. Closing this section on the mapping, we are now ready to formulate our DFT. The only remaining mapping parameter u_{pel}^0 will be determined within the DFT framework.

C. Density functional theory

Following previous studies [46,60], we consider two unit cells of a hexagonal lattice in a rectangular base with periodic boundary conditions in the x and y directions. The volume and the number of particles of the two unit cells are denoted by V_{cell} and N_{cell}, respectively. Our starting point is to construct a grand-canonical free-energy functional $\Omega([\rho(\vec{r})])$ whose value at its minimum corresponds to the equilibrium grand potential $\Omega_0(T, \mu, V; m, k_{\text{el}}, \eta_0, u_{\text{pel}}^0)$ in the grand-canonical ensemble at fixed temperature T, chemical potential μ, and volume V. The free parameters employed here are the magnitude of the magnetic moment m, the spring constant k_{el}, and the packing fraction η_0 of the reference system with $V_{\text{cell}} = N_{\text{cell}}V_0 = \sqrt{3}a^2$ as defined in Sec. II. In addition, we will complete the theory by specifying the yet to be determined offset for the pseudospring potential u_{pel}^0. As we have also employed an additional condition for n_{vac} in the preceding section, however, each resultant equilibrium density profile corresponds to a parameter set of $(m, k_{\text{el}}, \eta_0)$.

We write

$$\Omega([\rho(\vec{r})]) = \mathcal{F}([\rho(\vec{r})]) - \mu \int d\vec{r}\, \rho(\vec{r}), \tag{15}$$

where the Helmholtz free-energy functional $\mathcal{F} \equiv \mathcal{F}_{\text{id}}([\rho(\vec{r})]) + \mathcal{F}_{\text{exc}}([\rho(\vec{r})])$ consists of the ideal gas term and the excess functional, which read

$$\mathcal{F}_{\text{id}}([\rho(\vec{r})]) = \beta^{-1} \int d\vec{r}\, \rho(\vec{r})[\ln\{\Lambda^2 \rho(\vec{r})\} - 1],$$

$$\mathcal{F}_{\text{exc}}([\rho(\vec{r})]; m, k_{\text{el}}, \eta_0, u_{\text{pel}}^0) = \mathcal{F}_{\text{m}} + \mathcal{F}_{\text{el}} + \mathcal{F}_{\text{st}}, \tag{16}$$

respectively. Here Λ denotes the (here irrelevant) thermal wavelength. Regarding the elastic and magnetic interactions, we employ the mean-field functional in the form

$$\mathcal{F}_{\text{el,m}} \equiv \frac{1}{2} \int d\vec{r}\, d\vec{r}\,'\, \rho(\vec{r}) u_{\text{pel,m}}(|\vec{r} - \vec{r}\,'|)\rho(\vec{r}\,'), \tag{17}$$

while we adopt fundamental measure theory [46] for $\mathcal{F}_{\text{st}}$. Each excess functional is calculated with the aid of the Fourier convolution theorem. The detailed forms of the Fourier transforms of u_{pel} and u_{m} used in our calculations are described in Appendix A.

As in Refs. [46,48,61], we minimize Ω for a prescribed bulk density

$$\rho_{\text{bulk}} \equiv \frac{N_{\text{cell}}}{V_{\text{cell}}} = \frac{2(1 - n_{\text{vac}})}{V_{\text{cell}}}. \tag{18}$$

Here the chemical potential is obtained as an output of the calculation. Specifically, the minimization process consists of two distinct stages. At the first stage, we minimize $\mathcal{F}$ for fixed

n_{vac} using the Picard iteration algorithm

$$\rho^{(i+1)}(\vec{r}) = \alpha\tilde{\rho}^{(i)}(\vec{r}) + (1 - \alpha)\rho^{(i)}(\vec{r}), \quad (19)$$

with a mixing parameter α [44], where

$$\tilde{\rho}^{(i)}(\vec{r}) = \frac{1}{\Lambda^2}\exp\left[-\beta\frac{\delta\mathcal{F}_{\text{exc}}([\rho^{(i)}(\vec{r})])}{\delta\rho^{(i)}(\vec{r})} + \beta\mu^{(i)}\right]. \quad (20)$$

As we have prescribed the bulk density but not the chemical potential, $\mu^{(i)}$ is updated in each iteration step to keep the average density constant. Our convergence criterion for minimization at this stage is $(\mathcal{F}^{(i)} - \mathcal{F}^{(i+1)})/\mathcal{F}^{(i)} < 10^{-15}$, where $\mathcal{F}^{(i)} = \mathcal{F}([\rho^{(i)}(\vec{r})])$. Then we determine the equilibrium density profile by further minimizing $\mathcal{F}/N_{\text{cell}}$ with respect to n_{vac}. In practice, we vary n_{vac} by controlling V_{cell} while ρ_{bulk} is fixed. Comparing the values of $\mathcal{F}/N_{\text{cell}}$ obtained for each n_{vac}, we determine the vacancy concentration n_{vac} and the equilibrium density profile $\rho(\vec{r})$ with which the free energy per particle $\mathcal{F}/N_{\text{cell}}$ is minimized. These procedures are repeated until we have an accuracy of 10^{-6} for n_{vac}. In the calculations, we set $\Lambda = 1$.

Now we determine the values of u^0_{pel} to close our DFT. Specifically, we first perform the two-stage DFT minimization as discussed above to find corresponding vacancy concentrations for given values of u^0_{pel}. Then we choose the value of u^0_{pel} for which the vacancy concentration is zero, i.e., $n_{\text{vac}} = 0$. Apparently, the resultant offset values of u^0_{pel} and simultaneously the pseudopotential $u_{\text{pel}}(r_{ij})$ depend on the bulk density ρ_{bulk} of the system. According to Refs. [62,63], such a density dependence emerges as a consequence of introducing an effective potential between the individual particles in soft matter systems.

Performing first the minimization with $m = 0$ and without a hard-core repulsion ($\eta_0 = 0$), we confirm that the pseudospring potential indeed admits a freezing transition, which is the prerequisite of the mapping. Then we perform MC simulations with $\tilde{\mathcal{H}}_{\text{pel}}$, together with $\mathcal{H}_{\text{st}}$, to verify the mapping at finite packing fraction, using the value of u^0_{pel} obtained from such a DFT as an input. As manifested in Fig. 4, the agreement between the real-spring and the pseudospring systems is quantitatively excellent. Therefore, we conclude that the DFT approach to systems with labeled particles is successfully formulated with the pseudospring potential between unlabeled particles and ready to be used in the presence of magnetic interactions as a model for ferrogels.

IV. ELASTIC PROPERTIES OF FERROGELS

We finally demonstrate the utility of the theory to investigate the mechanical properties of ferrogels, varying the magnetic moment and the density of the particles. In particular, we probe the system at constant pressure $p = k_B T/a^2$ and determine the volume V and the responses to elastic deformations $\vec{\nabla}\vec{u}$, where $\vec{u}$ is the displacement field. With the component of the corresponding linear strain tensor [64]

$$\epsilon_{ij} = \tfrac{1}{2}(\vec{\nabla}_i u_j + \vec{\nabla}_j u_i), \quad (21)$$

the stress tensor and the stiffness tensor are defined as

$$\sigma_{ij} = \frac{\partial f}{\partial \epsilon_{ij}}, \quad C_{ijkl} = \frac{\partial \sigma_{ij}}{\partial \epsilon_{kl}}, \quad (22)$$

where $f \equiv F/V$ is the density of the Helmholtz free energy F. For two-dimensional hexagonal lattices, the stiffness tensor

$$C_{ijkl} = K\delta_{ij}\delta_{kl} + G(\delta_{ik}\delta_{jl} + \delta_{il}\delta_{jk} - \delta_{ij}\delta_{kl}) \quad (23)$$

can be expressed in terms of only two independent elastic constants, namely, the bulk modulus K and the shear modulus G, because of the symmetry [65].

In the following, we describe in Sec. IV A how to calculate the volume and elastic constants in MC simulations for the real-spring and pseudospring systems as well as using pseudopotentials from our DFT treatment. We compare the results of those methods in Sec. IV B. Henceforth, V and the elastic constants, namely, K and G, are measured in units of $NV_0 = N\sqrt{3}a^2/2$ and $k_B T/a^2$, respectively.

A. Implementation

1. MC simulation

In the case of MC simulations, we employ the isobaric-isothermal (TpN) ensemble [66,67] and vary the rectangular lengths L_x and L_y independently [68]. Accordingly, random walks in terms of $\ln L_x$ and $\ln L_y$ have been performed with the detailed balance condition [69]

$$\frac{\omega(V \to V')}{\omega(V' \to V)} = \exp\{-\beta[U(\vec{s}'^N, V') - U(\vec{s}^N, V)$$
$$+ p(V' - V)] + (N + 1)\ln(V'/V)\}, \quad (24)$$

where ω is the transition rate corresponding to the volume changes and $\vec{s}^N = \{\vec{s}_i\}$ are the scaled coordinates defined by $\vec{s}_i \equiv V^{-1/2}\vec{r}_i$ for $i = 1, \ldots, N$. We then compute the volumes of the systems, simply taking the average of $V \equiv L_x L_y$, and we extract K and G from the fluctuations $\langle(\Delta V)^2\rangle$, $\langle(\Delta L_x)^2\rangle$, and $\langle(\Delta L_y)^2\rangle$ [68]. The elastic constants are computed from the real-spring as well as the pseudospring MC simulations to verify the validity of the mapping. In particular, for the pseudospring MC simulation, we use the values of the offset u^0_{pel} obtained from the density functional calculations as inputs, while the average volumes extracted from the corresponding real-spring MC simulations are employed to determine the value of the cutoff R_c, with the aid of Eq. (14).

2. DFT calculation

Computation of thermodynamic quantities under the given pressure in DFT is formally not straightforward, because the theory is based on the grand-canonical ensemble. In a finite system, for example, the structure depends significantly on the specific choice of the statistical ensemble [70–72]. Due to the equivalence of the ensembles in the thermodynamic limit, however, one can still regard the density profiles obtained from DFT also as minima in the isobaric ensemble as long as large systems are considered. Hence, the requirement to compare the DFT results to MC simulations at constant pressure does not represent a conceptual problem for our study. Specifically, we first compute pressures at various volumes V_{cell} from the relation $p = -\Omega_0/V_{\text{cell}}$ and choose the volume at which the pressure reaches the prescribed value. The accuracy of the volume is $10^{-5}(2V_0)$ and the vacancy concentration is fixed during the procedures by fine-tuning u^0_{pel} with an

accuracy of $10^{-4} k_B T$. The detailed procedures are exemplified in Appendix B.

Since we have direct access to the free energy, we can directly compute the elastic constants deforming the system. We consider four types of deformations as follows:

$$\overset{\leftrightarrow}{\epsilon} = \begin{pmatrix} \epsilon_K & 0 \\ 0 & \epsilon_K \end{pmatrix}, \begin{pmatrix} \epsilon_x & 0 \\ 0 & 0 \end{pmatrix}, \begin{pmatrix} 0 & 0 \\ 0 & \epsilon_y \end{pmatrix}, \begin{pmatrix} \epsilon_G & 0 \\ 0 & -\epsilon_G \end{pmatrix}. \quad (25)$$

Specifically, we first deform the system according to the given strain, simultaneously controlling the density. Then we obtain the equilibrium density profile of the deformed system adjusting the vacancy concentration equivalently to the undeformed system as described in Sec. III C. We note that two types of deformation are enough to determine the two unknowns K and G. Examining four types of deformation, we verify the consistency of the theory. However, the deformations involving a volume difference seem to involve inelastic changes: Shifts of the vacancy concentration in the equilibrium step indeed imply changes in the number of particles in the unit cell, which would not occur during genuinely elastic deformations. To minimize such inelastic contributions, we utilize the identity $p \equiv -\Omega_0 / V_{\text{cell}}$ instead of directly computing the bulk modulus K from the definition of Eqs. (22) and (23). Specifically, the elastic constants are calculated from

$$K = -\frac{\{p(\epsilon_K) - p(0)\} + \{p(0) - p(-\epsilon_K)\}}{4\epsilon_K}, \quad (26)$$

$$G = \frac{f(\epsilon_G) + f(-\epsilon_G) - 2f(0)}{4\epsilon_G{}^2}, \quad (27)$$

where $f \equiv \mathcal{F}_0 / V_{\text{cell}}$ is the free-energy density, with the equilibrium free energy $\mathcal{F}_0$ of two unit cells computed from the two-step minimization process as described in Sec. III C. Here the pressure of the deformed systems is computed from $p(\epsilon_K) = -\Omega_0(\epsilon_K)/V_{\text{cell}}(\epsilon_K)$, where $\Omega_0(\epsilon_K)$ is the grand potential at which the density functional is minimized under the given constraint due to a deformation. We note that, in every case, the differences in the values of K are less than 10%, compared to the results for K that we have calculated in analogy to Eq. (27) via the changes in f, instead of using the pressure as in Eq. (26).

Before we proceed, let us make a few technical remarks. First, the minimization of the functionals at $n_{\text{vac}} = 0$ requires large computational resources because a small value of the Picard iteration parameter α in Eq. (19) should be used to guarantee the convergence of the minimization. To calculate the equilibrium density in a reasonable timescale, we choose to fix the iteration parameter at $\alpha = 0.001$ in general, at the cost of loosening the strict condition to impose a zero-vacancy concentration. Values of α smaller than that are only used for a few cases in which the minimization eventually fails otherwise. With this constraint, we could minimize the free-energy functional up to $n_{\text{vac}} = 0.0006 \pm 1.0 \times 10^{-6}$ for $\eta_0 = 0.3$ and 0.5 and $n_{\text{vac}} = 0.015 \pm 1.0 \times 10^{-6}$ for $\eta_0 = 0.8$. Second, as is well known, the numerical treatment of long-range interactions with periodic boundary conditions would require sophisticated techniques [73,74]. In the MC simulations we simply cut the magnetic interaction beyond the nearest-neighbor interaction as an approximation [26,75].
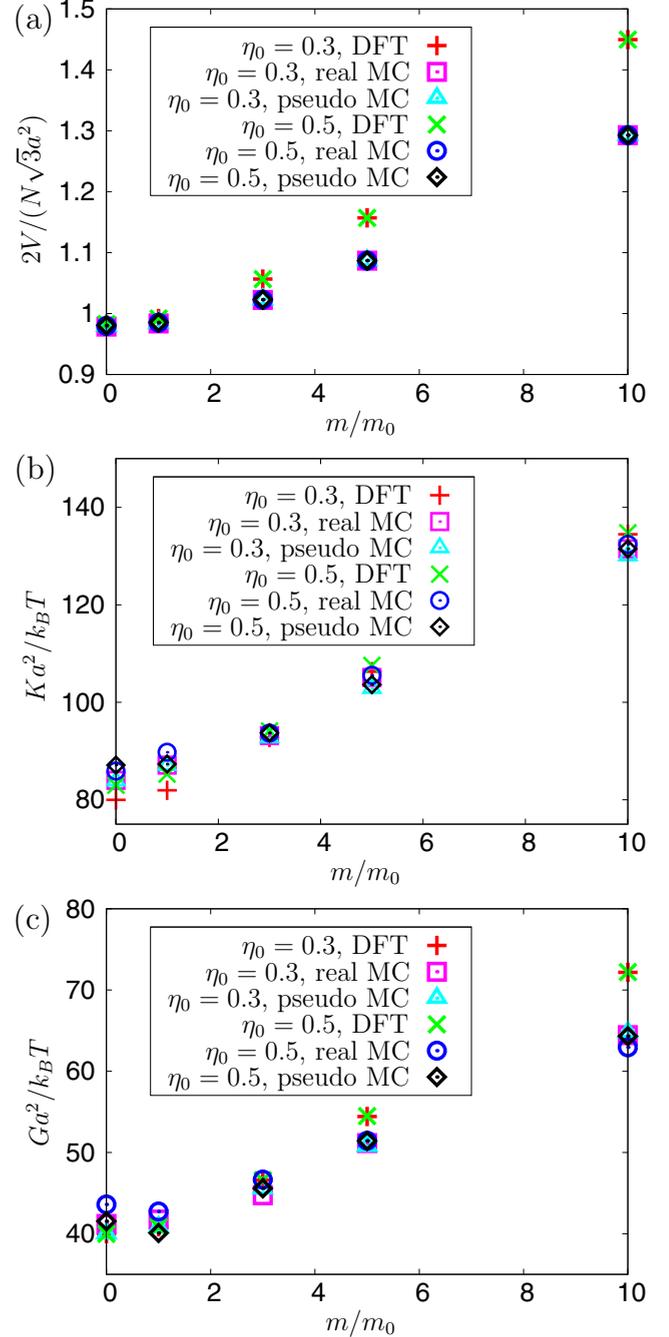
FIG. 5. For systems of low packing fractions, i.e., $\eta_0 = 0.3$ and 0.5, (a) the volume V, (b) the bulk modulus K, and (c) the shear modulus G are presented as functions of the repulsive magnetic dipole moment m. Apparently, the DFT overestimates the volume V for elevated values of m. Rough agreement among the theory and the MC simulations of both the real-spring and pseudospring systems are observed for both elastic constants K and G. Here $\epsilon_K = 0.00025$, $\epsilon_G = 0.00025$, and $N = 480$ have been used.

B. Results

We explore the following sets of parameters: $(k_{\text{el}}, \eta_0) = (100.0, 0.3)$, $(100, 0.5)$, and $(100.0, 0.8)$, each for several magnetic moments $m \leqslant 12$. Again, we note here that η_0
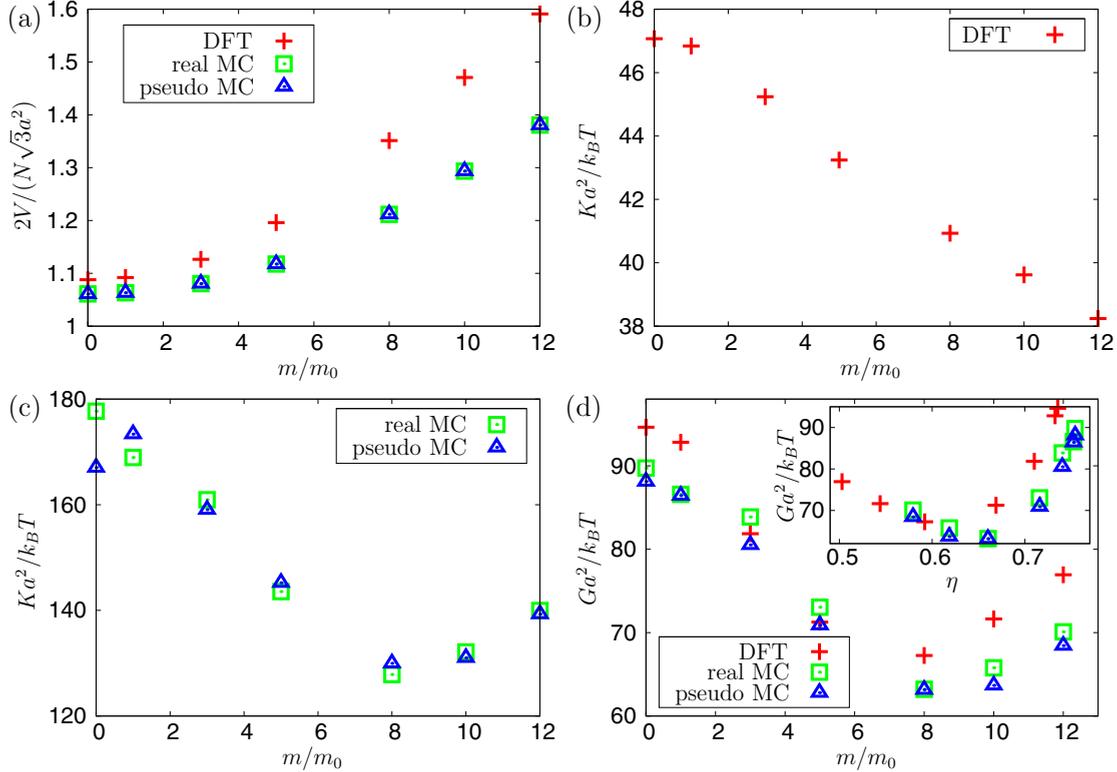
FIG. 6. For systems with a high packing fraction $\eta_0 = 0.8$, (a) the volume V, the bulk modulus K obtained from (b) DFT calculations and (c) MC simulations, and (d) the shear modulus G are presented as functions of the magnetic dipole moment m. As in Fig. 5, the DFT overestimates the volume V. For the elastic constants, the agreement among the theory, the real MC simulations, and the pseudo-MC simulations is again quite reasonable for the shear modulus G. However, the DFT significantly underestimates the bulk modulus K. The reason for this large deviation is very likely a rather large value of the vacancy concentration $n_{\rm vac} = 0.015$ (see the main text for details), but also the mean-field approximation may play a certain role. In the inset of (d), the values of the shear modulus are additionally presented as a function of the packing fraction $\eta \equiv (\pi \sigma^2/4) N/V$. Here $\epsilon_K = 0.00025$, $\epsilon_G = 0.00025$, and $N = 120$ have been used.

corresponds to the packing fraction of the reference system with $V = V_{\rm ref}$, conveying the information of the diameter of the particles. The conventional packing fraction is defined by $\eta \equiv (\pi \sigma^2/4) N/V$ and is not a fixed variable as we consider the isobaric ensemble [see the paragraph below Eq. (6) for details]. In Fig. 5 we first present the results at low packing fractions, i.e., $\eta_0 = 0.3$ and 0.5, for which the conventional hard-disk system is in the fluid phase [46,53,76]. Therefore, the crystallization in this low-packing-fraction regime is due to the elastic interaction. As one can see, the DFT and the real-spring and pseudospring MC simulations agree well with each other, except that the DFT overestimates the volumes, especially for large values of m. Here mean-field approximations adopted in our DFT and the truncation of the magnetic interaction in MC simulations seem to lead to such deviations between DFT and MC simulations. Overall, the volume V, the bulk modulus K, and the shear modulus G increase as the magnetic moment m increases.

Meanwhile, results with $\eta_0 = 0.8$ are shown in Fig. 6. In this case, we expect strong contributions from the steric forces. We first note that a significant deviation of the theory from the MC simulations in the bulk modulus is observed. Quantitatively, the bulk moduli obtained from the DFT are approximately one-fourth of those obtained from the MC simulations [compare Figs. 6(b) and 6(c)]. This seems to be

mostly due to the fact that we had to use a quite large value, i.e., $n_{\rm vac} \approx 0.015$, for the vacancy concentration because of technical reasons related to the computational time and the consequent choice of the mixing parameter α (see Sec. IV A). Indeed, using the same vacancy concentration, we also obtain similar deviations in K at $\eta_0 = 0.3$ or 0.5. Apart from that, the mean-field approximation may contribute to such deviations. Nonetheless, good agreement between the real-spring and pseudospring MC simulations is still observed, confirming that such a deviation of the DFT does not indicate a failure of our mapping. Surprisingly, the behavior of G is still well predicted by the DFT. In contrast to K, computation of G does not involve any changes in volume and consequently both the density and the vacancy concentration remain approximately constant during deformation. (In contrast to that, deformations involving volume changes are always accompanied by shifts of the vacancy concentration.) Therefore, we speculate that the vacancy concentration plays a much smaller role in the case of the volume-conserving deformation in DFT, for which $n_{\rm vac}$ remains basically the same. To conclude, except for the technical issue discussed, the DFT provides qualitatively correct trends even at high packing fractions.

Remarkably, we observe response behaviors of K and G to an increase in m for the high packing fraction, which are opposite to the low packing fraction. For $\eta_0 = 0.8$, K and

G decrease as m increases, while V is still an increasing function of m. The emergence of two such different scenarios originates from the composite nature of ferrogels: Here we are observing different types of crossovers from hard-disk crystals (high packing fraction, small m) or harmonic crystals (low packing fraction, small m) to elastic-dipolar crystals (both high and low packing fractions, large m).

To understand the phenomena in detail, we first note that V always increases as m increases because the magnetic interaction is repulsive. For low packing fractions, the magnetic repulsion simply causes additional increases in the bulk and shear moduli on top of the harmonic crystals. In contrast to that, for high packing fractions, the steric force dominates the mechanical properties and the system is very stiff (hard-disk crystals) with relatively large K and G for small values of m. As the magnetic moment m and consequently the volume V increase, the packing fraction η decreases and the contributions from the steric repulsion become insignificant compared to the dipolar repulsion at some values of the packing fraction around $0.6 \lesssim \eta \lesssim 0.7$ [see, e.g., the inset of Fig. 6(d)]. These values are slightly smaller than the fluid-crystal coexisting packing fractions of hard-disk systems, which are in between 0.68 and 0.73 [46,48,53,77,78]. Once η has decreased enough, as in the low-packing-fraction regime, the signature of the elastic-dipolar crystals should be recovered, the elastic properties of which are governed by the combination of the spring and dipolar interactions. Indeed, for $m = 10$, the volume and the elastic constants (compare Figs. 5 and 6) are quantitatively similar among $\eta_0 = 0.3$, 0.5, and 0.8. As expected, the values of K and G for $\eta_0 = 0.8$ increase in the regime of large magnetic moments, i.e., for $m \gtrsim 8$ where $\eta < 0.70$ ($\eta \approx 0.68$ and 0.60 for $m = 5$ and 8, respectively).

V. SUMMARY AND OUTLOOK

In this study we have formulated a DFT for a two-dimensional ferrogel model. We have replaced the labeled particles in a state of strictly permanently connected neighboring particles by the unlabeled particles in a fluidlike state to map the elastic part of the associated energy onto a pseudopotential invariant under permutations. In particular, we have shown that the mapping provides a plausible approximation for the considered systems and their response to magnetic interactions, even though the mapping still leads to some deviations in the calculated response of the systems. These deviations have been minimized by fine-tuning the mapping parameters. Finally, it has been demonstrated that the elastic properties of ferrogels can be successfully investigated in this framework and two scenarios have been identified for the response mechanism of the dipole-spring system, depending on the packing fraction. Notably, our DFT approach may also provide a clue for the scale bridging [79] between mesoscopic dipole-spring models and the macroscopic description of ferrogels [80,81]. In addition, a further extension to characterize other systems including many-body interactions [82–86] might be possible. Indeed, several of these studies assume certain lattice structures of particles, which is a prerequisite for our mapping.

A strong feature of the presented DFT approach relying on the pseudospring model in two dimensions is that it works well independently of the density. First of all, the mapping is generally well justified even in the low-density regime. Moreover, the mean-field DFT, which we employed here, provides a good approximation even in the high-density regime where we found good agreement between our theoretical treatment and MC simulations, especially for the shear modulus. In contrast to that, for a one-dimensional model, the prediction of unphysical freezing within mean-field DFT restricts the parameter space to intermediate densities and weaker elasticities [12], as otherwise the pseudospring approximation itself is less accurate due to large possible gaps between neighboring particles. We stress that, in general, mean-field approximations become more accurate with increasing dimensionality. Besides, true long-range order generally exists in three dimensions. Therefore, we expect our DFT approach to work even better in three dimensions.

Regarding possible experiments to test our theoretically predicted scenarios, the high packing fraction of $\eta_0 = 0.8$ needs to be discussed. As mentioned in Ref. [87], for certain systems there exists a region of increased mechanical stiffness around the magnetic particles. Effectively, this could be equivalent to an increased size of the particles. In addition, we note that in three dimensions, the fluid-crystal coexisting densities are reported as low as $\eta \approx 0.5$ [88,89]. Indeed, volume concentrations of approximately 50% have already been reported in three-dimensional samples of ferrogels [90], implying that the steric force should be taken into account explicitly. Therefore, decreasing elastic moduli in response to an increase of the magnitude of the magnetic moments might be observed in real three-dimensional systems. Furthermore, the pressure value employed in this study seems to be small: For instance, $p = k_B T / a^2 \sim 2 \times 10^{-7}$ Pa for the system studied in Ref. [19] with $a \approx 150$ nm at room temperature. Therefore, for direct comparison with experiments, a broad range of pressures should be explored in future studies with more realistic settings.

There are several remaining issues. First, aligning the magnetic dipoles within the two-dimensional plane and the resulting in-plane anisotropy will give rise to additional phenomena not observed here for perpendicular dipoles. To list a few, the aspect ratio of the width to the length of the unit cell will vary depending on the in-plane orientation of the magnetic dipole moments, the volume may change, and the magnetic particles could touch each other, leading to an abrupt change in elastic moduli even at a relatively low packing fraction [91]. The overall magnetization of ferrogels could also be of interest for further studies. For instance, rotational degrees of freedom of permanent magnetic dipoles in three dimensions [92,93] could explicitly be taken into account to investigate the relation between applied external magnetic fields and elastic moduli of ferrogels. Notably, in three-dimensional systems, the magnetic dipole interaction always leads to at least local anisotropy. As mentioned above, an extension to three dimensions would further strengthen the correspondence to real materials. Additionally, the mean-field functionals can be replaced by more sophisticated ones, especially to consider the long-range nature of the magnetic interaction [60]. Apart from that, the response dynamics to external magnetic fields represents another topic of interest. Dynamical DFT [51,94,95] should be the obvious candidate to study these phenomena in the present context.

APPENDIX A: FOURIER TRANSFORM

The functional derivatives of the mean-field functionals in Eq. (17) for the calculation of Eq. (20) read

$$\frac{\delta \mathcal{F}_{\text{el,m}}}{\delta \rho(\vec{r})} = \int d\vec{r}\,' \rho(\vec{r}\,') u_{\text{pel,m}}(|\vec{r} - \vec{r}\,'|), \qquad (A1)$$

which are numerically implemented with the aid of the convolution theorem. First, the Fourier transform of the elastic energy $\tilde{u}_{\text{pel}}$ can be computed as follows:

$$
\begin{aligned}
\tilde{u}_{\text{pel}}(\vec{k}) &= \int_0^{2\pi} d\theta \int_\sigma^{R_c} dr\, r\{\tfrac{1}{2}k_{\text{el}}(r-a)^2 - u_{\text{el}}^0\}e^{-i\vec{k}\cdot\vec{r}} \\
&= \int_\sigma^{R_c} dr\, 2\pi r J_0(kr)\{\tfrac{1}{2}k_{\text{el}}(r-a)^2 - u_{\text{el}}^0\} \\
&= \frac{\pi k_{\text{el}}}{k^3}[rJ_1(kr)\{-4 + k^2(r-a)^2 + ak\pi H_0(kr)\} \\
&\quad + rJ_0(kr)\{2kr - ak\pi H_1(kr)\}]_\sigma^{R_c} \\
&\quad - \frac{\pi u_{\text{el}}^0}{k}[2rJ_1(kr)]_\sigma^{R_c}.
\end{aligned}
\qquad (A2)
$$

Here J_i are the Bessel functions of the first kind of order i and H_i the Struve functions of order i. For the magnetic interaction, the Fourier transformation can be performed as

$$
\begin{aligned}
\tilde{u}_{\text{m}}(\vec{k}) &= \frac{\mu_0 m^2}{4\pi} \int_\sigma^\infty dr \int_0^{2\pi} d\theta \frac{1}{r^2}e^{-i\vec{k}\cdot\vec{r}} \\
&= \frac{\mu_0 m^2}{2} \int_\sigma^\infty dr \frac{J_0(kr)}{r^2} \\
&= \frac{\mu_0 m^2}{2}\left[-\frac{1}{r}\,{}_1F_2\left(-\frac{1}{2};\frac{1}{2},1;-\frac{1}{4}k^2r^2\right)\right]_\sigma^\infty,
\end{aligned}
\qquad (A3)
$$

TABLE I. Example of the DFT computation procedure. Here $ka^2/k_B T = 100$, $\eta_0 = 0.3$, and $R_c^0/a = 1.34$.

$V_{\text{cell}}/N_{\text{cell}}V_0$	$u_{\text{pel}}^0/k_B T$	n_{vac}	$pa^2/k_B T$
0.98250	2.7419	0.0006002	
	2.7420	0.0006000	1.000609
	2.7421	0.0005999	
0.98251	2.7422	0.0006002	
	2.7423	0.0006000	0.999613
	2.7424	0.0005998	

where ${}_1F_2$ is the generalized hypergeometric function. For $r \to \infty$,

$$
\begin{aligned}
{}_1F_2&\left(-\frac{1}{2};\frac{1}{2},1;-\frac{1}{4}k^2r^2\right) \\
&= kr + \frac{\cos kr - \sin kr}{\sqrt{\pi}k^{3/2}}r^{-3/2} + O(r^{-5/2}).
\end{aligned}
\qquad (A4)
$$

We finally obtain

$$\tilde{u}_{\text{m}}(\vec{k}) = \frac{\mu_0 m^2}{2}\left[-k + \frac{1}{\sigma}\,{}_1F_2\left(-\frac{1}{2};\frac{1}{2},1;-\frac{k^2\sigma^2}{4}\right)\right]. \quad (A5)$$

The generalized hypergeometric functions were implemented using the ARB library [96].

APPENDIX B: DFT MINIMIZATION

In this Appendix we describe the procedure of computing the equilibrium profile at prescribed pressure within the grand-canonical DFT, which is exemplified in Table I. First, the volume V_{cell} and the offset u_{pel}^0 are fixed (the first and the second column in Table I). We then compute the free energy per particle $\mathcal{F}/N_{\text{cell}}$, varying the vacancy concentration n_{vac} (the third column). At this stage, we control n_{vac} by changing V_{cell} while fixing the density ρ_{bulk} [see Eq. (18)]. We choose the value of u_{pel}^0 for which $\mathcal{F}/N_{\text{cell}}$ is minimized at the prescribed value of the vacancy concentration (for the parameter set in Table I, $n_{\text{vac}} = 0.0006$). At this stage, the pressure corresponding to the fixed volume is determined simultaneously (the fourth column). Now we change the volume, varying the density ρ_{bulk} while fixing the number of particles N_{cell}, and repeat the above procedure to calculate corresponding pressures. Finally, we obtain the volume and corresponding density profile, comparing pressures with the prescribed pressure value, i.e., $pa^2/k_B T = 1$.

[1] R. K. Pathria, *Statistical Mechanics* (Butterworth-Heinemann, Boston, 1996), pp. 22–26.

[2] M. Kardar, *Statistical Physics of Particles* (Cambridge University Press, Cambridge, 2007).

[3] K. Huang, *Introduction to Statistical Physics* (Chapman and Hall/CRC, Boca Raton, 2009).

[4] M. E. Cates and V. N. Manoharan, Soft Matter **11**, 6538 (2015).

[5] J. Sethna, *Statistical Mechanics: Entropy, Order Parameters, and Complexity* (Oxford University Press, Oxford, 2006), Vol. 14.

[6] R. H. Swendsen, Entropy **10**, 15 (2008).

[7] D. Frenkel, Mol. Phys. **112**, 2325 (2014).

[8] E. T. Jaynes, Phys. Rev. **106**, 620 (1957).

[9] E. T. Jaynes, *Maximum Entropy and Bayesian Methods* (Springer, Berlin, 1992), pp. 1–21.

[10] M. Doi and S. F. Edwards, *The Theory of Polymer Dynamics* (Clarendon, Oxford, 1986).

[11] A. M. Menzel, Arch. Appl. Mech. **89**, 17 (2019).

[12] P. Cremer, M. Heinen, A. M. Menzel, and H. Löwen, J. Phys.: Condens. Matter **29**, 275102 (2017).

[13] T. Schindler, R. Wittmann, and J. M. Brader, Phys. Rev. E **99**, 012605 (2019).

[14] G. Filipcsei, I. Csetneki, A. Szilágyi, and M. Zrínyi, Adv. Polymer Sci. **206**, 137 (2007).

[15] P. Ilg, Soft Matter **9**, 3465 (2013).

[16] T. Gundermann and S. Odenbach, Smart Mater. Struct. **23**, 105013 (2014).

[17] J. Landers, L. Roeder, S. Salamon, A. M. Schmidt, and H. Wende, J. Phys. Chem. C **119**, 20642 (2015).

[18] N. Frickel, R. Messing, and A. M. Schmidt, J. Mater. Chem. **21**, 8466 (2011).

[19] R. Messing, N. Frickel, L. Belkoura, R. Strey, H. Rahn, S. Odenbach, and A. M. Schmidt, Macromolecules **44**, 2990 (2011).

[20] L. Roeder, P. Bender, M. Kundt, A. Tschöpe, and A. M. Schmidt, Phys. Chem. Chem. Phys. **17**, 1290 (2015).

[21] G. V. Stepanov, D. Y. Borin, Y. L. Raikher, P. V. Melenev, and N. S. Perov, J. Phys.: Condens. Matter **20**, 204121 (2008).

[22] O. V. Stolbov, Y. L. Raikher, and M. Balasoiu, Soft Matter **7**, 8484 (2011).

[23] O. V. Stolbov and Y. L. Raikher, Arch. Appl. Mech. **89**, 63 (2019).

[24] G. Pessot, H. Löwen, and A. M. Menzel, J. Chem. Phys. **145**, 104904 (2016).

[25] G. Pessot, M. Schümann, T. Gundermann, S. Odenbach, H. Löwen, and A. M. Menzel, J. Phys.: Condens. Matter **30**, 125101 (2018).

[26] S. Goh, A. M. Menzel, and H. Löwen, Phys. Chem. Chem. Phys. **20**, 15037 (2018).

[27] A. M. Biller, O. V. Stolbov, and Y. L. Raikher, J. Appl. Phys. **116**, 114904 (2014).

[28] A. M. Biller, O. V. Stolbov, and Y. L. Raikher, Phys. Rev. E **92**, 023202 (2015).

[29] P. Cremer, H. Löwen, and A. M. Menzel, Appl. Phys. Lett. **107**, 171903 (2015).

[30] P. Cremer, H. Löwen, and A. M. Menzel, Phys. Chem. Chem. Phys. **18**, 26670 (2016).

[31] M. Puljiz, S. Huang, G. K. Auernhammer, and A. M. Menzel, Phys. Rev. Lett. **117**, 238003 (2016).

[32] M. Puljiz and A. M. Menzel, Phys. Rev. E **95**, 053002 (2017).

[33] R. Weeber, S. Kantorovich, and C. Holm, Soft Matter **8**, 9923 (2012).

[34] R. Weeber, S. Kantorovich, and C. Holm, J. Magn. Magn. Mater. **383**, 262 (2015).

[35] R. Weeber, P. Kreissl, and C. Holm, Arch. Appl. Mech. **89**, 3 (2019).

[36] N. Goldenfeld, *Lectures on Phase Transitions and the Renormalization Group* (Addison-Wesley, Urbana-Champaign, 1992), Chap. 2.

[37] N. Ashcroft and N. Mermin, *Solid State Physics* (Holt, Rinehart & Winston, New York, 1976).

[38] R. Evans, Adv. Phys. **28**, 143 (1979).

[39] J. F. Lutsko, Adv. Chem. Phys. **144**, 1 (2010).

[40] R. Evans, M. Oettel, R. Roth, and G. Kahl, J. Phys.: Condens. Matter **28**, 240401 (2016).

[41] H. Löwen, J. Phys.: Condens. Matter **14**, 11897 (2002).

[42] C. Ebner, W. F. Saam, and D. Stroud, Phys. Rev. A **14**, 2264 (1976).

[43] T. V. Ramakrishnan and M. Yussouff, Phys. Rev. B **19**, 2775 (1979).

[44] R. Roth, J. Phys.: Condens. Matter **22**, 063102 (2010).

[45] R. Wittmann, M. Marechal, and K. Mecke, J. Phys.: Condens. Matter **28**, 244003 (2016).

[46] R. Roth, K. Mecke, and M. Oettel, J. Chem. Phys. **136**, 081101 (2012).

[47] R. Wittmann, C. E. Sitta, F. Smallenburg, and H. Löwen, J. Chem. Phys. **147**, 134908 (2017).

[48] S.-C. Lin and M. Oettel, Phys. Rev. E **98**, 012608 (2018).

[49] U. Zimmermann, F. Smallenburg, and H. Löwen, J. Phys.: Condens. Matter **28**, 244019 (2016).

[50] R. Roth and D. Gillespie, J. Phys.: Condens. Matter **28**, 244006 (2016).

[51] A. J. Archer and R. Evans, J. Chem. Phys. **121**, 4246 (2004).

[52] E. P. Bernard, W. Krauth, and D. B. Wilson, Phys. Rev. E **80**, 056704 (2009).

[53] M. Engel, J. A. Anderson, S. C. Glotzer, M. Isobe, E. P. Bernard, and W. Krauth, Phys. Rev. E **87**, 042134 (2013).

[54] L. Tonks, Phys. Rev. **50**, 955 (1936).

[55] J. K. Percus, J. Stat. Phys. **15**, 505 (1976).

[56] K. Zahn and G. Maret, Phys. Rev. Lett. **85**, 3656 (2000).

[57] P. Keim, G. Maret, U. Herz, and H. H. von Grünberg, Phys. Rev. Lett. **92**, 215504 (2004).

[58] N. D. Mermin and H. Wagner, Phys. Rev. Lett. **17**, 1133 (1966).

[59] B. Jancovici, Phys. Rev. Lett. **19**, 20 (1967).

[60] S. van Teeffelen, H. Löwen, and C. N. Likos, J. Phys.: Condens. Matter **20**, 404217 (2008).

[61] M. Oettel, S. Görig, A. Härtel, H. Löwen, M. Radu, and T. Schilling, Phys. Rev. E **82**, 051404 (2010).

[62] A. A. Louis, P. G. Bolhuis, J. P. Hansen, and E. J. Meijer, Phys. Rev. Lett. **85**, 2522 (2000).

[63] A. A. Louis, J. Phys.: Condens. Matter **14**, 9187 (2002).

[64] L. D. Landau and E. M. Lifshitz, *Theory of Elasticity* (Elsevier, Oxford, 1986).

[65] P. M. Chaikin and T. C. Lubensky, *Principles of Condensed Matter Physics* (Cambridge University Press, Cambridge, 2000).

[66] W. W. Wood, J. Chem. Phys. **48**, 415 (1968).

[67] R. Eppenga and D. Frenkel, Mol. Phys. **52**, 1303 (1984).

[68] D. H. Boal, U. Seifert, and J. C. Shillcock, Phys. Rev. E **48**, 4274 (1993).

[69] D. Frenkel and B. Smit, *Understanding Molecular Simulation*, 2nd ed. (Academic, San Diego, 2002).

[70] A. González, J. A. White, F. L. Román, S. Velasco, and R. Evans, Phys. Rev. Lett. **79**, 2466 (1997).

[71] A. González, J. A. White, F. L. Román, and S. Velasco, J. Chem. Phys. **120**, 10634 (2004).

[72] D. de las Heras, J. M. Brader, A. Fortini, and M. Schmidt, J. Phys.: Condens. Matter **28**, 244024 (2016).

[73] M. P. Allen and D. J. Tildesley, *Computer Simulation of Liquids* (Oxford University Press, Oxford, 2017).

[74] A. Arnold and C. Holm, in *Advanced Computer Simulation Approaches for Soft Matter Sciences II*, edited by C. Holm and K. Kremer (Springer, Berlin, 2005), pp. 59–109.

[75] A. Daddi-Moussa-Ider, S. Goh, B. Liebchen, C. Hoell, A. J. T. M. Mathijssen, F. Guzmán-Lastra, C. Scholz, A. M. Menzel, and H. Löwen, J. Chem. Phys. **150**, 064906 (2019).

[76] C. H. Mak, Phys. Rev. E **73**, 065104(R) (2006).

[77] E. P. Bernard and W. Krauth, Phys. Rev. Lett. **107**, 155704 (2011).

[78] A. L. Thorneywork, J. L. Abbott, D. G. A. L. Aarts, and R. P. A. Dullens, Phys. Rev. Lett. **118**, 158001 (2017).

[79] A. M. Menzel, J. Chem. Phys. **141**, 194907 (2014).

[80] E. Jarkova, H. Pleiner, H.-W. Müller, and H. R. Brand, Phys. Rev. E **68**, 041706 (2003).

[81] S. Bohlius, H. R. Brand, and H. Pleiner, Phys. Rev. E **70**, 061411 (2004).

[82] D. C. Morse and T. A. Witten, Europhys. Lett. **22**, 549 (1993).

[83] M.-D. Lacasse, G. S. Grest, D. Levine, T. G. Mason, and D. A. Weitz, Phys. Rev. Lett. **76**, 3448 (1996).

[84] M.-D. Lacasse, G. S. Grest, and D. Levine, Phys. Rev. E **54**, 5436 (1996).

[85] R. Höhler and S. Cohen-Addad, Soft Matter **13**, 1371 (2017).

[86] L. Athanasopoulou and P. Ziherl, Soft Matter **13**, 1463 (2017).

[87] S. Huang, G. Pessot, P. Cremer, R. Weeber, C. Holm, J. Nowak, S. Odenbach, A. M. Menzel, and G. K. Auernhammer, Soft Matter **12**, 228 (2016).

[88] W. G. Hoover and F. H. Ree, J. Chem. Phys. **49**, 3609 (1968).

[89] R. Roth, R. Evans, A. Lang, and G. Kahl, J. Phys.: Condens. Matter **14**, 12063 (2002).

[90] T.-Y. Liu, S.-H. Hu, K.-H. Liu, D.-M. Liu, and S.-Y. Chen, J. Control. Release **126**, 228 (2008).

[91] M. A. Annunziata, A. M. Menzel, and H. Löwen, J. Chem. Phys. **138**, 204906 (2013).

[92] D. S. Wood and P. J. Camp, Phys. Rev. E **83**, 011402 (2011).

[93] P. J. Camp, Magnetohydrodynamics **47**, 123 (2011).

[94] U. M. B. Marconi and P. Tarazona, J. Chem. Phys. **110**, 8032 (1999).

[95] D. Stopper, A. L. Thorneywork, R. P. A. Dullens, and R. Roth, J. Chem. Phys. **148**, 104501 (2018).

[96] F. Johansson, IEEE Trans. Comput. **66**, 1281 (2017).